

Multiscale Waves in an MJO Background and Convective Momentum Transport Feedback

BOUALEM KHOUIDER AND YING HAN

Department of Mathematics and Statistics, University of Victoria, Victoria, British Columbia, Canada

ANDREW J. MAJDA

*Center for Atmosphere–Ocean Science, and Department of Mathematics, Courant Institute,
New York University, New York, New York*

SAMUEL N. STECHMANN

Department of Mathematics, University of Wisconsin—Madison, Madison, Wisconsin

(Manuscript received 1 June 2011, in final form 23 September 2011)

ABSTRACT

The authors use linear analysis for a simple model to study the evolution of convectively coupled waves (CCWs) in a background shear and background moisture mimicking the observed structure of the Madden–Julian oscillation (MJO). This is motivated by the observation, in an idealized setting, of intraseasonal two-way interactions between CCWs and a background wind. It is found here that profiles with a bottom-heavy moisture content are more favorable to the development of mesoscale/squall line–like waves whereas synoptic-scale CCWs are typically more sensitive to the shear strength. The MJO envelope is thus divided into three regions, in terms of the types of CCWs that are favored: an onset region in front that is favorable to Kelvin waves, a mature or active region in the middle in which squall lines are prominent, and the stratiform and decay phase region in the back that is favorable to westward inertia–gravity (WIG) waves. A plausible convective momentum transport (CMT) feedback is then provided according to the results of the idealized two-way interaction model. The active region, in particular, coincides with the westerly wind burst where both Kelvin waves and squall lines are believed to play a significant role in both the deceleration of low-/high-level easterly/westerly winds and the acceleration of low-/high-level westerly/easterly winds. The WIG waves in the wake could be a precursor for a subsequent MJO event through the acceleration of low-/high-level easterly/westerly winds, which in turn favor Kelvin waves, and the cycle repeats. These results open interesting directions for future studies using observations and/or detailed numerical simulations using the full primitive equation.

1. Introduction

The Madden–Julian oscillation (MJO; Madden and Julian 1971, 1972) is a planetary-scale disturbance of winds and enhanced convection that travels eastward at about 5 m s^{-1} in the tropical troposphere, over the Indian and the western Pacific oceans. Various studies have confirmed the multiscale organization of tropical convection into a hierarchy of temporal and spatial

scales ranging from propagating mesoscale cloud clusters to synoptic- and planetary-scale (the MJO) wave disturbances that share a self-similar structure and are embedded in each other like Russian dolls (Nakazawa 1988; Mapes et al. 2006). The zonal wind and temperature anomalies are characterized by a front-to-rear vertical tilt (Kiladis et al. 2009) with easterlies below westerlies in front and westerlies below easterlies in the rear of the convection center and with warm temperatures preceding cold temperatures at low levels while warm temperatures prevail in the upper troposphere in the center and somewhat to the rear of the deep convection center. This vertical structure is believed to be supported by the succession of three cloud types.

Corresponding author address: Dr. Boualem Khouider, Dept. of Mathematics and Statistics, University of Victoria, P.O. Box 3045, STN CSC, Victoria BC V8W 3P4, Canada.
E-mail: khouider@math.uvic.ca

Cumulus congestus clouds in front heat the lower troposphere and cool the upper troposphere, deep convection in the center serves to heat the entire troposphere, and a wake of stratiform anvils warms the upper rear of the wave and cools it below (Johnson et al. 1999; Kiladis et al. 2005; Mapes et al. 2006; Kiladis et al. 2009).

It is now widely recognized that the synoptic-scale disturbances are the moist equivalent of the equatorially trapped waves of Matsuno (1966) with a very complex coupling between various vertical baroclinic modes through convection and moisture, resulting in the vertical tilt mentioned above and a significantly reduced phase speed (Kiladis et al. 2009). While Nakazawa (1988) is perhaps the first to reveal the existence of a hierarchy of clusters and superclusters embedded within the MJO, using satellite data, recent detailed studies of two individual MJO events during the Tropical Ocean Global Atmosphere Coupled Ocean–Atmosphere Response Experiment (TOGA COARE) (Lin and Johnson 1996; Chen et al. 1996; Moncrieff and Klinker 1997; Yanai et al. 2000; Houze et al. 2000) have shed light onto the dominant effect of squall line–like convective bands that move in the direction of the low-level wind from both ends of the MJO convection center. These lines of convection have the capability of converting convectively available energy at the convective scale to kinetic energy, resulting in either damping or acceleration of the ambient vertical shear (LeMone 1983; LeMone et al. 1998; Tung and Yanai 2002a,b).

The transfer of momentum from the convective to synoptic and planetary scales is known in the literature as convective momentum transport (CMT). Here we abusively call CMT the transport of momentum from a circulation feature that is associated with convective organization on of a certain scale to a larger scale, including the transfer of momentum from mesoscale systems to synoptic and to planetary scales and from synoptic-scale superclusters to planetary scales.

In addition to the observational evidence for the significance of CMT from mesoscale convective systems, there are also a few theoretical and numerical studies that addressed this issue (Moncrieff 1981; Dudhia et al. 1987; Moncrieff 1992; LeMone and Moncrieff 1994; Wu and Yanai 1994; Liu and Moncrieff 1996; Wu and Moncrieff 1996; Majda and Stechmann 2008, 2009a, hereafter MS09; Lane and Moncrieff 2010; Khouider et al. 2012). An interesting overview perspective can be found in the introduction section of MS09.

The other important form of CMT consists in transferring momentum from synoptic-scale convectively coupled waves (CCWs) to planetary scales. Synoptic-

planetary-scale CMT is the main energy source in the multiscale (kinematic) MJO model of Majda and Biello (2004) whereas in Biello and Majda (2005) it competes with planetary-scale heating; it is believed to constitute the “muscle” of the MJO while the planetary-scale heating is part of its “skeleton,” to paraphrase Majda and Stechmann (2009b), who proposed the first idealized model for the MJO that reproduces most of its dominant features. However, while the role of the background shear and background thermodynamics in controlling the dynamics of mesoscale squall lines is well established, the evolution of synoptic-scale waves in the MJO, for instance, is poorly understood. Except for the case of dry waves evolving in a prescribed background shear, very few observational and/or theoretical studies have addressed this issue (Haertel and Johnson 1998; Roundy 2008; Han and Khouider 2010, hereafter HK10; MS09).

Based on the multicloud model of Khouider and Majda (2006, 2008a,b), MS09 proposed and analyzed a multiscale asymptotic model for the dynamical interactions between a background vertical shear and synoptic-scale CCWs. In these studies, the multicloud model carries two vertical modes of vertical structure, forced by convective heating from the three cloud types (congestus, deep, and stratiform) that characterize the heating field of tropical convective systems (Johnson et al. 1999). It assumes a uniform radiative cooling and is coupled to vertically averaged tropospheric moisture and to the boundary layer equivalent potential temperature but the nonlinear advection terms are ignored. In the MS09 framework, the background vertical shear forces packets of CCWs through advection and the CCWs provide in return a CMT feedback that changes the strength and direction of the background shear on an intraseasonal time scale mimicking the acceleration and deceleration phases of the MJO westerly wind burst (WWB). As a result the CCWs undergo drastic changes in strength and direction of propagation due to the dependence of their growth rates and phase speeds on the background vertical shear, according to linear analysis (MS09). Although the Coriolis force is ignored, the MS09 model provides an interesting paradigm for the two-way interactions between the MJO WWB and the embedded CCWs. Moreover, the linear analysis of MS09 in particular showed that while sometimes the most unstable synoptic-scale CCWs move in the direction opposite to the low-level background wind, the model also exhibits mesoscale squall line–like moist gravity waves that propagate with the low-level background wind. This is consistent with the evolution of squall lines in the TOGA COARE MJO background (LeMone et al. 1998). In the remainder of the paper, we

will abusively call “squall line” any type of mesoscale CCWs that has a phase speed roughly equal to the maximum of the low-level background wind, known as the steering-level wind (Moncrieff 1992).

The evolution of CCWs in a prescribed vertical and meridional background shear, using the multcloud model on a beta plane (Khouider and Majda 2008a) without CMT feedback, is studied in HK10. The same kind of dependence of the wave growth rates and phase speeds on the shear strength and wind direction is reported but the picture is much more complex as it involves the whole menagerie of equatorially trapped waves: Kelvin, westward and eastward inertia–gravity (WIG and EIG), mixed Rossby–gravity (MRG), and Rossby waves. The results of HK10 showed the same sensitivity of the stability characteristics of CCWs in the multcloud model to the background vertical shear. It is shown in HK10 that both low-level (WWB-like) and high-level westerlies destabilize convectively coupled Kelvin waves, consistent with the observational analysis of Roundy (2008), who showed that Kelvin waves persist in both the active (WWB) and inactive (low-level easterly) phase of the MJO. However, WIG and EIG waves in the multcloud model follow mainly high-level easterlies and high-level westerlies, respectively. This led the authors to conjecture that Kelvin waves are more likely to persist in both the active and inactive phases of the MJO while WIG waves are more likely to occur within the active (WWB) phase of the MJO. Besides these interesting discoveries, the work of HK10 did not reveal instabilities of squall line–like waves as in MS09, unlike the TOGA COARE data that showed an abundance of such mesoscale features on both sides of the MJO envelopes that propagate in the direction of the midlevel shear.

While vertical wind shears mimicking the evolution of both the low-level easterlies and low-level westerlies in the front and in the rear of the MJO envelope, respectively, were considered in HK10, they carry only the first and second baroclinic components. This is motivated by the fact that these are the only vertical structure modes that are directly excited by the three cloud types of tropical convection (Khouider and Majda 2006). However, the background wind in MS09 comprises the three first baroclinic modes, with the third mode being directly forced by CMT fluxes. We can thus conjecture that the lack of squall line–like mesoscale waves in the work of HK10 is due to the lack of a third baroclinic zonal wind component in the prescribed background vertical shear. One physical explanation for this could be attributed to the fact that the third mode affects directly the strength of the low-level shear, which is known to induce squall lines (see, e.g., Moncrieff 1992; MS09). In

this paper, we extend the linear theory analysis of HK10 to the case of a more realistic MJO background zonal wind that involves all the three first baroclinic components. We consider both the CCWs CMT-forced WWB-like mean vertical shear obtained in the multiscale simulation of MS09 at various times spanning its life cycle and a sequence of zonal shears sampled throughout the life cycle of an MJO event from reanalysis data (Tromeur and Rossow 2010). As expected, in both cases we obtain squall line–like instabilities in addition to the menagerie of equatorial CCWs.

The rest of the article is organized as follows. In section 2, we introduce the multcloud model governing equations linearized around a zonal wind background, with a vertical shear, that includes the three first baroclinic components; discuss the multiscale model of MS09; and proceed with the linear wave analysis for the multcloud model, on a beta plane, using the MS09 zonal wind background shear. While the zonal wind vertical shear is perhaps the most apparent variable within the MJO envelope, CCWs are sensitive to the thermodynamic backgrounds. A more realistic MJO background mimicking reanalysis data in both zonal wind and moisture profiles is considered in section 3. Section 4 presents an MJO scenario where changes in zonal wind vertical shear are combined with moisture profile variations throughout the MJO life cycle. The types of multiscale CCWs that are unstable in various regions of the MJO envelope are obtained together with some speculations for a plausible CMT feedback on the MJO. The paper concludes with a short summary in section 5.

2. The multcloud model in a background shear and the two-way interaction model of MS09

In this work, we consider the multcloud model on an equatorial beta plane, linearized about a zonal wind background vertical shear with three baroclinic components (MS09; HK10), at radiative–convective equilibrium (RCE):

$$\bar{\mathbf{V}}(z, \tau) = \sum_{j=1}^3 [\bar{U}_j(\tau), 0] \cos(jz), \quad (1)$$

where $0 \leq z \leq \pi$ is the height coordinate normalized so that $z = 0$ is at the surface and $z = \pi$ is at the top of the troposphere and τ is a slow time (see below). For the purpose of the linear analysis in sections 3 and 4, it can be thought of the MJO lag time.

$$\begin{aligned}
\frac{\partial u_1}{\partial t} - \frac{\partial \theta_1}{\partial x} - yv_1 + \frac{\sqrt{2}}{2} \left(3\bar{U}_1 \frac{\partial u_2}{\partial x} + 3\bar{U}_2 \frac{\partial u_1}{\partial x} + \frac{1}{2}\bar{U}_1 \frac{\partial v_2}{\partial y} + 2\bar{U}_2 \frac{\partial v_1}{\partial y} + \frac{5}{2}\bar{U}_3 \frac{\partial u_2}{\partial x} + \frac{3}{2}\bar{U}_3 \frac{\partial v_2}{\partial y} \right) &= -\frac{C_d u_0}{h_b} u_1 - \frac{1}{\tau_D} u_1 \\
\frac{\partial u_2}{\partial t} - \frac{\partial \theta_2}{\partial x} - yv_2 + \frac{\sqrt{2}}{2} \left(-\bar{U}_1 \frac{\partial v_1}{\partial y} + 4\bar{U}_3 \frac{\partial u_1}{\partial x} + 3\bar{U}_3 \frac{\partial v_1}{\partial y} \right) &= -\frac{C_d u_0}{h_b} u_2 - \frac{1}{\tau_D} u_2 \\
\frac{\partial v_1}{\partial t} - \frac{\partial \theta_1}{\partial y} + yu_1 + \frac{\sqrt{2}}{2} \left(\bar{U}_1 \frac{\partial v_2}{\partial x} + \bar{U}_2 \frac{\partial v_1}{\partial x} + \bar{U}_3 \frac{\partial v_2}{\partial x} \right) &= -\frac{C_d u_0}{h_b} v_1 - \frac{1}{\tau_D} v_1 \\
\frac{\partial v_2}{\partial t} - \frac{\partial \theta_2}{\partial y} + yu_2 + \frac{\sqrt{2}}{2} \left(\bar{U}_1 \frac{\partial v_1}{\partial x} + \bar{U}_3 \frac{\partial v_1}{\partial x} \right) &= -\frac{C_d u_0}{h_b} v_2 - \frac{1}{\tau_D} v_2 \\
\frac{\partial \theta_1}{\partial t} - \left(\frac{\partial u_1}{\partial x} + \frac{\partial v_1}{\partial y} \right) + \frac{\sqrt{2}}{2} \left(2\bar{U}_1 \frac{\partial \theta_2}{\partial x} - \bar{U}_2 \frac{\partial \theta_1}{\partial x} - 2\bar{U}_3 \frac{\partial \theta_2}{\partial x} \right) + \frac{\sqrt{2}}{8} (-yv_2 \bar{U}_1 + 2yv_1 \bar{U}_2 + 3yv_2 \bar{U}_3) &= H_d + \xi_s H_s + \xi_c H_c \\
&\quad - Q_{R,1}^0 - \frac{1}{\tau_R} \theta_1 \\
\frac{\partial \theta_2}{\partial t} - \frac{1}{4} \left(\frac{\partial u_2}{\partial x} + \frac{\partial v_2}{\partial y} \right) + \frac{\sqrt{2}}{4} \left(\bar{U}_1 \frac{\partial \theta_1}{\partial x} - \bar{U}_3 \frac{\partial \theta_1}{\partial x} \right) + \frac{\sqrt{2}}{4} (yv_1 \bar{U}_1 + 3yv_1 \bar{U}_3) &= H_c - H_s - Q_{R,2}^0 \\
&\quad - \frac{1}{\tau_R} \theta_2 \\
\frac{\partial q}{\partial t} + \alpha_1 \bar{U}_1 \frac{\partial q}{\partial x} + \alpha_2 \bar{U}_2 \frac{\partial q}{\partial x} + \alpha_3 \bar{U}_3 \frac{\partial q}{\partial x} + \tilde{Q} \left(\frac{\partial u_1}{\partial x} + \frac{\partial v_1}{\partial y} \right) + \tilde{\lambda} \tilde{Q} \left(\frac{\partial u_2}{\partial x} + \frac{\partial v_2}{\partial y} \right) &= -\frac{2\sqrt{2}}{\pi} (H_d + \xi_s H_s \\
&\quad + \xi_c H_c) + \frac{1}{H_T} D \\
\frac{\partial \theta_{eb}}{\partial t} + \sqrt{2} \left(\bar{U}_1 \frac{\partial \theta_{eb}}{\partial x} + \bar{U}_2 \frac{\partial \theta_{eb}}{\partial x} + \bar{U}_3 \frac{\partial \theta_{eb}}{\partial x} \right) &= \frac{1}{\tau_e} (\theta_{eb}^* - \theta_{eb}) - \frac{D}{h_b} \\
\frac{\partial H_s}{\partial t} - \frac{32\sqrt{2}}{15\pi} \left(\bar{U}_1 \frac{\partial H_s}{\partial x} \right) + \frac{32\sqrt{2}}{21\pi} \left(\bar{U}_3 \frac{\partial H_s}{\partial x} \right) &= \frac{1}{\tau_s} [\alpha_s H_d - H_s] \\
\frac{\partial H_c}{\partial t} + \frac{32\sqrt{2}}{15\pi} \left(\bar{U}_1 \frac{\partial H_c}{\partial x} \right) + \frac{32\sqrt{2}}{21\pi} \left(\bar{U}_3 \frac{\partial H_c}{\partial x} \right) &= \frac{1}{\tau_c} \left[\alpha_c \Lambda \frac{1}{H_T} D - H_c \right].
\end{aligned} \tag{2}$$

Here u_j , v_j , and θ_j , where $j = 1, 2$, are the components of the first and second baroclinic modes of vertical structures of the zonal velocity, the meridional velocity, and the potential temperature, respectively. Also, q is the vertically averaged specific humidity and θ_{eb} is the boundary layer equivalent potential temperature; H_d , H_s , and H_c are the heating and cooling rates due respectively to deep convection, stratiform anvils, and congestus clouds, while $Q_{R,1}^0$ and $Q_{R,2}^0$ are the radiative cooling rates associated with the first and second baroclinic modes, respectively. Finally, D is the downdraft mass flux that includes the cooling effect from stratiform rain that falls into a dry lower troposphere and evaporates, and θ_{eb}^* is the saturation θ_{eb} while τ_e is the evaporation time scale from the sea surface. The rest of parameters and closure assumptions of the multicloud model are listed in Table 1 for convenience. More details can be found in Khouider and Majda (2006) and subsequent papers on the multicloud model.

The advective terms in the θ_1 and θ_2 equations that involve the Coriolis gradient βy ($\beta = 1$ here) are due to the meridional advection of the background potential temperature Θ by the synoptic-scale meridional velocities where the geostrophic balance/thermal wind equations $\partial_y \Theta_j = yU_j$, with $j = 1, 2, 3$ were used. We note, however, that these terms induce only small quantitative changes to the results and therefore can be neglected. For a similar reason the vertical advection of the background temperature is actually neglected in those equations because it is even smaller, on the order of $(y)^2$.

Unless otherwise stated, all equations and variables are given in nondimensional units where the length scale is roughly 1500 km (the equatorial Rossby radius of deformation), the velocity scale is 50 m s^{-1} (the phase speed of the first baroclinic Kelvin wave), the time scale is 8.33 h, and the temperature scale is 15 K. These units are chosen so that the Coriolis beta parameter and the temperature stratification gradient are set to one (Majda

TABLE 1. Closures and parameters of the multicloud model.

Variable/parameter	Closure/value	Description
H_d	$(1 - \Lambda) \left\{ \bar{Q}_c + \frac{1}{\tau_{\text{conv}}} [a_1 \theta_{eb} + a_2 q - a_0 (\theta_1 + \gamma_2 \theta_2)] \right\}^+$	Deep convective heating
$Q_{R,1}$	1 K day ⁻¹	First baroclinic radiative cooling rate
$Q_{R,2}$	Determined at RCE	Second baroclinic cooling rate
τ_R	50 days	Newtonian cooling time scale
τ_D	75 days	Rayleigh friction time scale
\bar{Q}_c	Determined at RCE	Background convective heating at RCE
D	$D = \left(1 + \mu \frac{H_s - H_c}{\bar{Q}_{R,1}} \right)^+ (\theta_{eb} - \theta_{em})$	Downdrafts
θ_{eb}^*	Undetermined	Saturation equivalent potential temperature
θ_{em}	$\bar{\theta}_{em} + q + \sqrt{2} \pi (\theta_1 + \alpha_2 \theta_2)$	Middle tropospheric equivalent potential temperature
$\theta_{eb}^* - \bar{\theta}_{eb}$	10 K	Discrepancy between θ_{eb}^* and θ_{eb} value at RCE
$\bar{\theta}_{eb} - \bar{\theta}_{em}$	11 K	Discrepancy between boundary layer and middle tropospheric θ_e
Λ	1 if $\theta_{eb} - \theta_{em} > 20$ K 0 if $\theta_{eb} - \theta_{em} < 10$ K Linear continuous otherwise	Moisture switch function
a_1	0.25	Deep convection parameter
a_2	0.75	Deep convection parameter
a_0	3	Deep convection parameter
γ_2	0.1	Deep convection parameter
α_2	0.1	Relative contribution of θ_2 in the θ_{em}
μ	0.25	Downdraft parameter
\tilde{Q}	0.9 (changes)	First baroclinic moisture convergence background
$\tilde{\lambda}$	0.8 (changes)	Second baroclinic moisture convergence background
τ_s	3 h	Stratiform adjustment time
τ_c	1 h	Congestus adjustment time
τ_{conv}	2 h	Convective time scale
α_s	0.16	Stratiform adjustment fraction
α_c	0.1	Congestus adjustment fraction

2003). Moisture is converted to temperature units based on the latent heat of vaporization and heat capacity of dry air, under normal atmospheric conditions (Khouider and Majda 2006).

a. The multiscale model of MS09

To allow two-way interactions between the synoptic-scale convectively coupled waves and a slowly varying background flow, the MS09 model assumes that the flow field decomposes into two components that vary on two different time scales. In terms of the baroclinic modes of vertical structure for the zonal velocity, this amounts to setting

$$u_j^{\text{tot}}(x, y, t, \tau) = U(\tau) + \epsilon u_j(x, y, t), \quad j = 1, 2, 3, \dots$$

Here $\tau = \epsilon^2 t$ is a slow time scale with $\epsilon = 0.1$ so that when t varies on the synoptic scale (8.33 h), τ adopts the intraseasonal time scale of roughly 34 days. For convectively coupled waves in the multicloud model, where only the first and second baroclinic modes are present, the slowly varying background zonal velocity carries

three baroclinic modes, U_1 , U_2 , and U_3 , that are directly forced by CMT while the associated background potential temperature carries four baroclinic modes Θ_j , $j = 1, 2, 3, 4$ (MS09). The governing equations for U_1 , U_2 , and U_3 are given by (MS09)

$$\begin{aligned} \frac{dU_1}{d\tau} &= -\frac{1}{\sqrt{2}} \left\langle u_2 \frac{\partial u_1}{\partial x} - \frac{1}{2} u_1 \frac{\partial u_2}{\partial x} \right\rangle, \\ \frac{dU_2}{d\tau} &= 0, \\ \frac{dU_3}{d\tau} &= \frac{3}{\sqrt{2}} \left\langle u_2 \frac{\partial u_1}{\partial x} + \frac{1}{2} u_1 \frac{\partial u_2}{\partial x} \right\rangle, \end{aligned} \quad (3)$$

when the Coriolis force and the meridional dependence are neglected (which is assumed in this section only). The angle brackets in (3) are the time averages with respect to the synoptic time scale t and the overbars denote the running zonal average. It is interesting to note here that the second baroclinic components of the background wind are not forced directly by CMT while, as observed in MS09 (but not explicitly stated), U_1 and

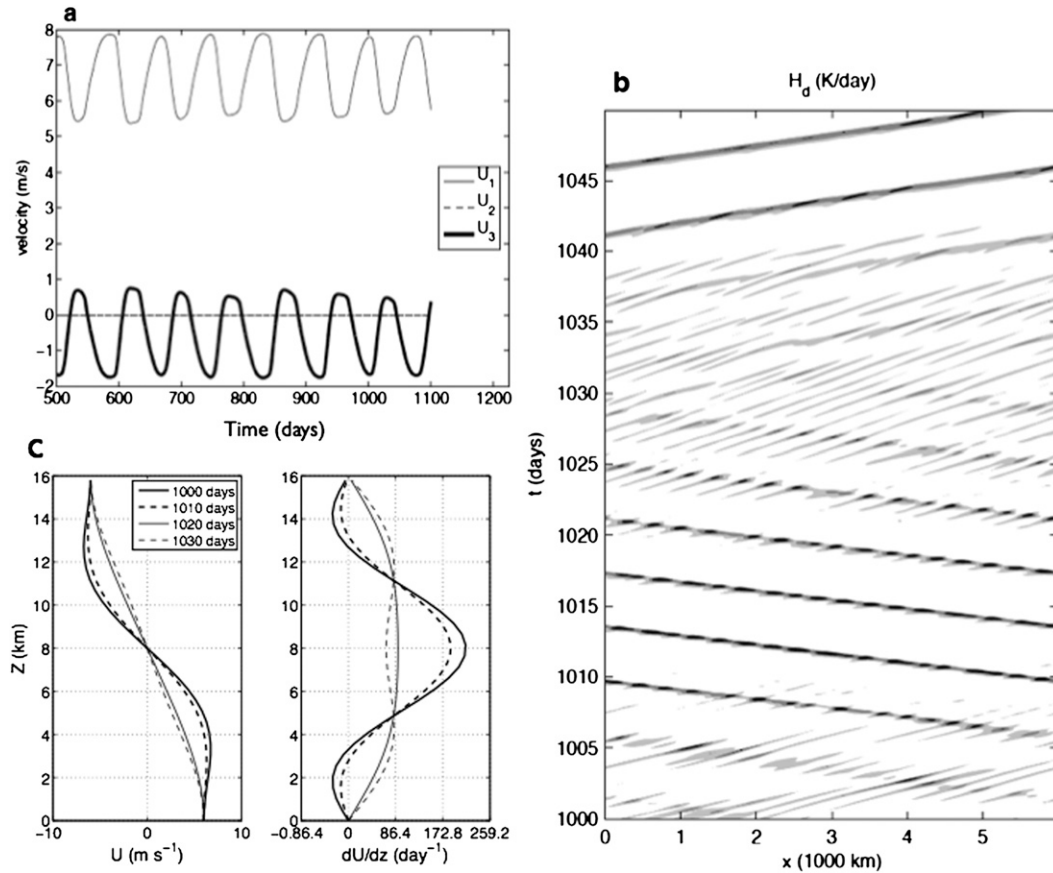


FIG. 1. Two-way interactions between a background westerly wind and convectively coupled gravity waves in the multcloud model in the 2D domain over the equator. (a) Time history of background zonal wind components. (b) Hovmöller diagram of deep convection H_d for the synoptic-scale waves. (c) Vertical profile of the total background wind at various times during a deceleration phase together with the corresponding shear profile (see text for details). Adopted from MS09.

U_3 satisfy $dU_1/d\tau = -dU_3/d\tau$. This can be easily established by noting that $u_2(\partial u_1/\partial x) - 1/2[u_1(\partial u_2/\partial x)] = 3/2[u_2(\partial u_1/\partial x)] - 1/2[\partial(u_1 u_2)/\partial x]$ and $3\{u_2(\partial u_1/\partial x) + 1/2[u_1(\partial u_2/\partial x)]\} = 3/2\{u_2(\partial u_1/\partial x) + 3/2[\partial(u_1 u_2)/\partial x]\}$ and that $\partial(u_1 u_2)/\partial x = 0$.

In MS09, the equations in (3) are coupled to the multcloud equations in (2) in the simple case without rotation (where the meridional velocity and y dependence are ignored) and solved numerically on a periodic domain of 6000 km using a discretization procedure adapted to the multiple time scales. In the case when the background mean flow is such that $|U_1| \gg |U_3|$ and $U_2 = 0$ (initially), the coupled system exhibits irregular intraseasonal oscillations with an average period of roughly 80 days. In Fig. 1, we show (a) the time history plots of the background flow components U_1 and U_3 that display irregular intraseasonal oscillations during which the westerly wind accelerates and decelerates, (b) the space–time (Hovmöller) contour plot of the synoptic-scale zonal velocity during the deceleration period that occurs

roughly between 1000 and 1040 days, and (c) a sequence of the reconstructed vertical profiles of the background mean wind $U(z) = U_1\sqrt{2}\cos(z) + U_2\sqrt{2}\cos(2z) + U_3\sqrt{2}\cos(3z)$ at various times during the deceleration phase together with the corresponding shear profile $U_z(z) = -U_1\sqrt{2}\sin(z) - 2U_2\sqrt{2}\sin(2z) - 3U_3\sqrt{2}\sin(3z)$. Note that U_1 , U_2 , and U_3 are functions of the slow time only (i.e., independent of x) that are treated as constant parameters in the linear analysis in sections 2b, 3, and 4, which permits us to study the effects of the “evolving” background flow on the synoptic and mesoscale waves but it does not allow CMT feedback from these waves on the background flow.

As we can see from Fig. 1 (see also MS09), the major effect of the background wind variability is to change the direction of propagation of the convectively coupled gravity waves while the westward- and eastward-propagating waves provide, respectively, deceleration and acceleration fluxes for the low (high)-level westerly (easterly) shear through CMT. As the shear weakens the

synoptic-scale waves change their direction of propagation from west to east. The transition periods between eastward and westward wave propagation are dominated by short-lived squall line–like mesoscale waves that move in the direction of the low-level wind (i.e., eastward). While the direction of propagation of the mesoscale waves is consistent with the general theory and observations of squall lines (Moncrieff 1981; Dudhia et al. 1987; Moncrieff 1992), the synoptic CCWs seem to trigger their own demise by disfavoring their favorable background; while the strong shear is favorable for westward waves and the weak shear favors eastward waves, westward-moving waves seem to decelerate the westerly shear while eastward waves seem to accelerate it. Nonetheless, these results were corroborated by linear analysis. It is shown in MS09 that in the weak WWB background, corresponding roughly to the profile at day 1030 in Fig. 1, the multicloud model has instabilities of both eastward- and westward-moving synoptic-scale waves but the eastward waves have stronger growths whereas in the “fully developed” strong WWB shear, which also exhibits strong high-level easterlies, westward-moving waves are more unstable. This is consistent with the results of HK10, who showed that, in the case with rotation, WIG waves are favored by high-level easterlies and Kelvin waves are destabilized by both high-level and low-level westerlies. In the case without rotation, considered in MS09, there is a perfect symmetry between eastward and westward propagation of gravity waves. One can thus conjecture that in the case of easterlies over westerlies, weak westerly shear backgrounds would favor the propagation of eastward (Kelvin-like) waves while strong westerly shear backgrounds would favor westward (WIG-like) waves. This is indeed confirmed in the case with rotation in section 2b below but in the case of westerlies over easterlies (mimicking the MJO onset region) the picture is different: both the weak and strong shears are more favorable for eastward-moving waves (i.e., Kelvin and EIG waves). This is in fact consistent with the results of HK10 mentioned above. Moreover, the linear results of MS09 showed that eastward-moving mesoscale waves are unstable in both the strong and weak WWB backgrounds, which explains the persistence of squall line–like waves during the transition periods between eastward- and westward-moving waves in Fig. 1.

b. Linear theory on a beta plane with the MS09 shear background

In this section we test the mean shear background of the previous section on a beta plane. Namely, we perform linear stability analysis for the multicloud equations in (2) when the background wind $U(z) = U_1\sqrt{2}\cos(z) + U_2\sqrt{2}\cos(2z) + U_3\sqrt{2}\cos(3z)$ is given by the sequence

of decelerating westerly wind bursts from the simulation of MS09 shown on the bottom-left panel of Fig. 1. Here we investigate the effect of these background wind profiles on convectively coupled waves when the rotation effects are included without taking into account the CMT feedback effect from such waves on the background wind. The background wind itself is kept independent of y and thus meridional variations in that direction that may result from CMT feedback or any other effects are ignored here.

The solution methodology is the same as in HK10 except for the fact that here the background wind includes a third baroclinic component; solutions on the form of linear waves

$$\mathbf{u}(x, y, t) = \sum_{j=0}^N \hat{\mathbf{u}}_j \phi_j(y) e^{i(kx - \omega t)},$$

with $N = 15$, are sought. Here $\phi_j(y)$, $j = 1, \dots, N$ are the parabolic cylinder functions, k is the zonal wavenumber, and ω is the generalized (complex) frequency whose real part $\Re(\omega)$ is the phase and imaginary part $\Im(\omega)$ is the growth rate of the wave.

1) WESTERLIES BELOW EASTERLIES

In Fig. 2, we plot the symmetric dispersion relations—that is, the phase versus the zonal wavenumber—for the decelerating sequence wind profiles on the bottom-left panel of Fig. 1. For each (fixed) wavenumber the system has a certain number of wave-mode frequencies corresponding to the number of prognostic variables in the Galerkin expanded system, which is separated into symmetric and antisymmetric parts. Among the frequency curves, in the various panels in Fig. 2, there are analogs of the equatorially trapped modes, such as the Kelvin, Rossby, and inertia–gravity waves of lower meridional indices (limited by the level of the Galerkin truncation), and many other modes that are induced by the boundary layer, moisture, and congestus and stratiform heating equations [see Khouider and Majda (2008a) and HK10 for details]. While only results from the symmetric part of the truncated system are presented and analyzed here, the antisymmetric part exhibits a fairly similar behavior although the overall growth rates are slightly smaller; the Kelvin wave is replaced by the eastward MRG (Yanai) wave and the antisymmetric gravity waves by their symmetric counterparts. Thus, the antisymmetric part of the wave spectrum is omitted throughout the paper for the sake of streamlining.

In Fig. 2, the wavenumber bands of instability are highlighted on the corresponding branches by the small filled circles of various sizes that are proportional to the growth rate (HK10). In addition, some of the instability and wave features are summarized in Table 2

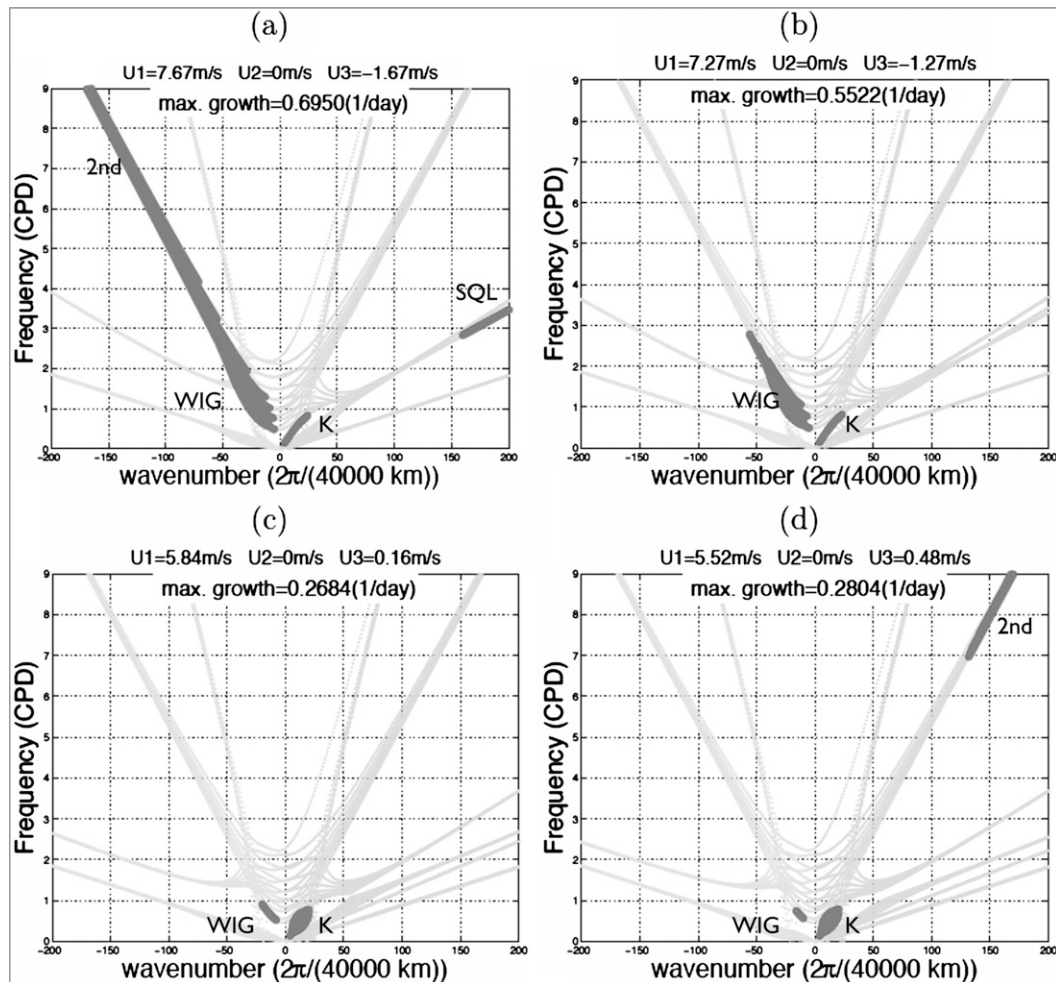


FIG. 2. Dispersion relations for the multicloud model with a sequence of vertical WWB-like background shears from the MS09 model results in Fig. 1 at (a) 1000, (b) 1010, (c) 1020, and (d) 1030 days, representing a deceleration phase of the low-level westerly wind. We note that the reversed sequence amounts to the acceleration phase. The strength of the baroclinic components of the background wind is indicated on top of each panel. The bands of instability are highlighted with small circles. The size of each small circle is proportional to the corresponding relative growth rate in each panel where the maximum growth rate is indicated as a reference. The unstable branches are marked: K (Kelvin), WIG/EIG (westward/eastward inertia-gravity), 2nd (dry second baroclinic wave), and SQL (squall line-like mode).

(columns marked “WW”). Figure 2 and Table 2 show that as the westerly wind decelerates, it progressively transits from a state (at time 1000 days) that is favorable to synoptic-scale WIG waves, with a growth maximum around $k = 23$, to a state (at time 1030 days) that is more favorable to Kelvin waves peaking around $k = 13$. We note that whereas during the WIG wave-favorable phase Kelvin waves have a growth rate that is small but comparable (roughly 2 times smaller) to that of the WIG waves, in the Kelvin wave regime the growth peak of the WIG waves is 5 times smaller than that of the Kelvin waves.

These results are roughly consistent with those in HK10 according to which strong high-level easterlies destabilize WIG waves while Kelvin waves are unstable

in the presence of both high- and low-level westerlies. But there are many important new features. In addition, we see in Fig. 2 mesoscale instabilities of eastward- and westward-moving waves, peaking roughly around $k = 200$, with phase speeds of 8 and 25 m s^{-1} , which correspond, respectively, to roughly the maximum speeds of the low-level wind, consistent with the propagation of squall lines in the TOGA COARE MJO (LeMone 1983; Moncrieff 1981; Tung and Yanai 2002a,b, etc.) and the phase speed of the dry second baroclinic gravity waves (at large wavenumber). Moreover, the physical and dynamical structure (not shown here) of the 25 m s^{-1} waves project heavily on the second baroclinic modes and resemble those of dry gravity waves in terms of

TABLE 2. Growth and phase speed at the peak on instability for the wind profiles from the MS09 model during the deceleration phase from Fig. 1. The WW/EW column displays the results related to westerly/easterly wind at the surface; “2nd” denotes an instability of a dry second baroclinic wave mode.

Time (days)	\bar{U} (m s ⁻¹)		Waves		Growth (day ⁻¹) (wavenumber)		Phase speed (m s ⁻¹)	
	WW	EW	WW	EW	WW	EW	WW	EW
1000	$U_1 = 7.67,$ $U_3 = -1.67$	$U_1 = -7.67,$ $U_3 = 1.67$	WIG	Kelvin	0.695 (25)	0.806 (24)	-21.4	19.8
			2nd modes (W)	2nd modes (E)	0.167 (200)	0.167 (200)	-25	25
			Kelvin	EIG	0.233 (14)	0.61 (14)	17.6	26
			Squall line	Squall line	0.055 (200)	0.055 (200)	8	-8
1010	$U_1 = 7.27,$ $U_3 = -1.27$	$U_1 = -7.27,$ $U_3 = 1.27$	WIG	Kelvin	0.552 (22)	0.675 (21)	-21.4	19.35
			Kelvin	EIG	0.235 (14)	0.47 (21)	17.7	26
1020	$U_1 = 5.84,$ $U_3 = 0.16$	$U_1 = -5.84,$ $U_3 = -0.16$	WIG	Kelvin	0.111 (14)	0.284 (14)	-22.5	18.1
			Kelvin	EIG	0.268 (13)	0.1 (10)	18.2	26
1030	$U_1 = 5.52,$ $U_3 = 0.48$	$U_1 = -5.52,$ $U_3 = -0.48$	WIG	Kelvin	0.032 (13)	0.212 (13)	-23	17.85
			Kelvin	EIG	0.28 (13)	0.05 (10)	18.3	30
			2nd modes (E)	2nd modes (W)	0.046 (200)	0.046 (200)	25	-24.6
1040	$U_1 = 5.63,$ $U_3 = 0.37$	$U_1 = -5.63,$ $U_3 = -0.37$	WIG	Kelvin	0.0575 (13)	0.237 (13)	-23	17.9
			Kelvin	EIG	0.276 (13)	0.06 (10)	18.3	30
			2nd modes (E)	2nd modes (W)	0.0215 (200)	0.0215 (200)	25	-25

wind and temperature anomalies in addition to the fact that their heating and moisture anomalies are relatively weaker. Sensitivity tests, not included here, showed that these mesoscale instabilities are due to the presence of the third baroclinic background wind component.

In the MS09 simulation, the deceleration of the background westerly shear is caused by the westward-moving waves that are tilted backward with respect to the surface wind direction. However, the squall lines and the EIG (and especially the Kelvin) waves move in the same direction as the surface wind and therefore they are tilted in such a way as to accelerate the WWB. Thus, such back and forth transitions may contribute to the MJO initiation, maintenance, and propagation. However, while MS09 considered the background westerly shear in Fig. 1 to mimic the westerly wind burst in the active phase of the MJO, the MJO wave itself comprises both easterly (easterly winds below westerly winds) and westerly (westerlies below easterlies) shears, in its front (inactive phase) and rear, respectively. If one assumes some kind of symmetry within the MJO wave, then a close representation of the wind shear in front of the MJO convection can be obtained by simply considering the negative of the background shear presented in Fig. 1 and used in Fig. 2. This is totally legitimate in the MS09 model. Since the effects of rotation were ignored, there is a perfect symmetry between eastward and westward gravity wave propagation.

2) WESTERLIES OVER EASTERLIES

In Fig. 3, we repeat the results of Fig. 2 but for a sequence of low-level (high-level) easterly (westerly) shears obtained by taking the negative of the WWB sequence in Fig. 1. See also Table 2 (columns marked “EW”). From

Fig. 3 and Table 2, we see that unlike in the WW case, here no dramatic change in stability behavior is noticeable; the EW remains favorable for Kelvin and EIG waves throughout the deceleration phase. However, as expected the corresponding instability is stronger (in terms of both growth rates and band of instability) for the strongest shear. Moreover, we have mesoscale westward-moving squall line–like (moving at 8 m s⁻¹) and eastward-moving second baroclinic gravity wave instabilities when the low-level shear is at its maximum (Fig. 3a) and westward second baroclinic gravity waves when the shear is the weakest (Fig. 3d): a mirror image of the WW case.

3) WAVE STRUCTURE

The structures of the convectively coupled synoptic-scale waves of Figs. 2 and 3 and Table 2 are identical to those shown in HK10 (with a vertical shear) and therefore they are not repeated here. The structure of the mesoscale squall line–like wave is shown in Fig. 4. The structure of the westward-moving squall line (associated with the westerlies over easterlies background) is identical to that in Fig. 4 except for the fact that it is tilted eastward and that its zonal flow is more confined to the equatorial region.

Consistent with the fact that rotation effects are negligible at small scales, the structure of these mesoscale waves, including the 25 m s⁻¹ second baroclinic gravity waves, is more or less independent of the direction of propagation, at least qualitatively. In fact, all of them displayed a horizontal structure resembling that of the Kelvin wave. This is consistent with the fact that the theoretical eigenstructure of the inertia–gravity waves of equatorial shallow water theory (e.g., Majda 2003) predicts a meridional to zonal velocity ratio that scales

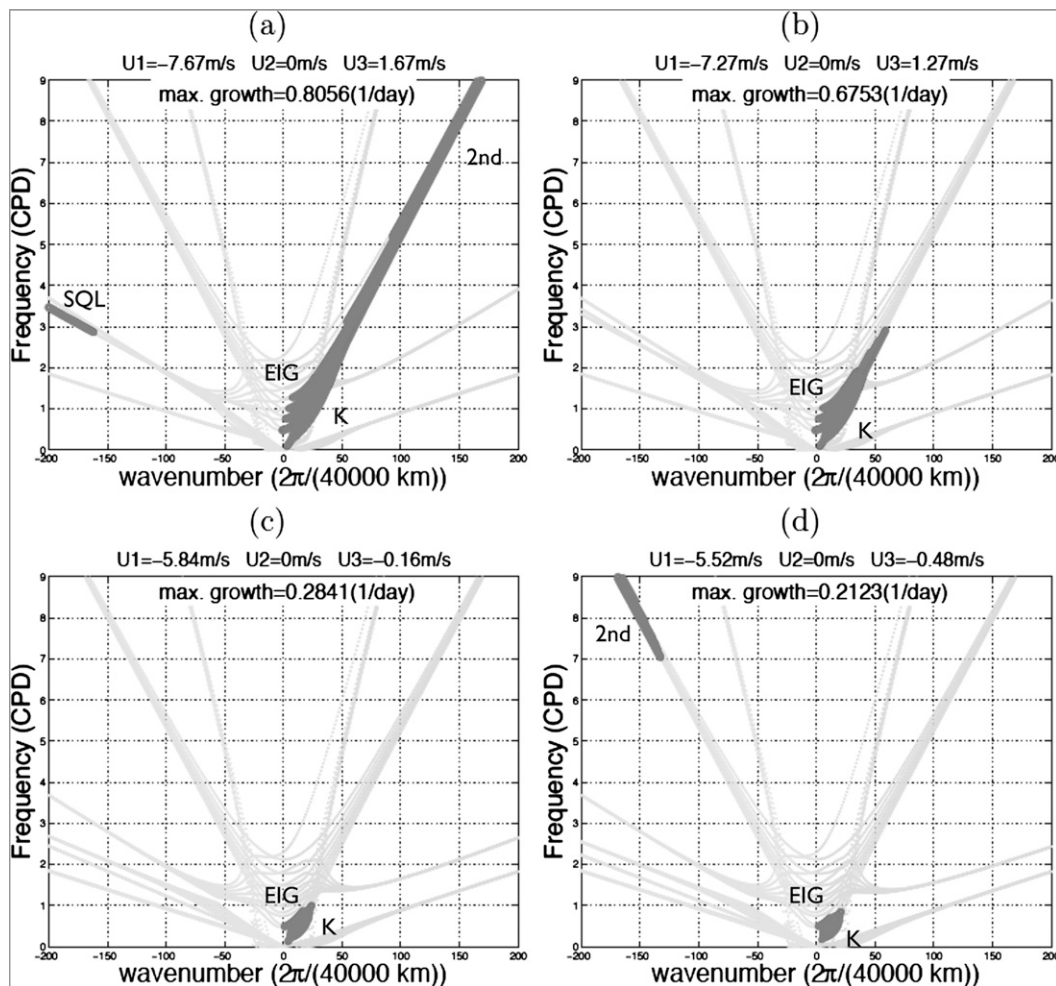


FIG. 3. As in Fig. 2, but for low-level easterly background mimicking the deceleration of the dry phase/onset phase of the MJO.

as $1/k$. However, the squall lines seem to be more trapped in the vicinity of the equator than the second baroclinic waves and the westward squall lines are especially more trapped than their eastward counterparts. The main structural and physical differences between the squall lines and the second baroclinic waves can be summarized as follows. 1) The velocity and potential temperature fields of the squall lines are dominated by the first baroclinic mode while the second baroclinic mode dominates in the second case. 2) While in the dry second baroclinic gravity waves the velocity and potential temperature fields are relatively strong compared to the moisture variables, the squall line physical structure is dominated by q and θ_{eb} . 3) While in both types of waves, the heating field is dominated by upright deep convection, the vertical structure of the squall lines display a bottom-heavy and strongly tilted temperature profile consistent with the domination in strength of moisture

and boundary layer temperature, as shown in Fig. 4. There is an appreciable vertical tilt in zonal velocity as well but it is somewhat hard to distinguish from the wind profile in Fig. 4. However, this does not imply that its CMT effect on the MJO is negligible. In fact, in the simulations of Khouider et al. (2012), who used a parameterization to account for the CMT effect from unresolved mesoscale features, the tilt in the zonal and vertical wind of the subgrid mesoscale features is very weak, in the sense that it is hard to distinguish on the wave picture (just like in Fig. 4), but the CMT effect, especially, on the MJO-like planetary-scale wave is very significant, according to the simulation results.

3. Realistic MJO background

Here, we extend our analysis to more realist MJO background shears. Specifically, we consider a sequence of

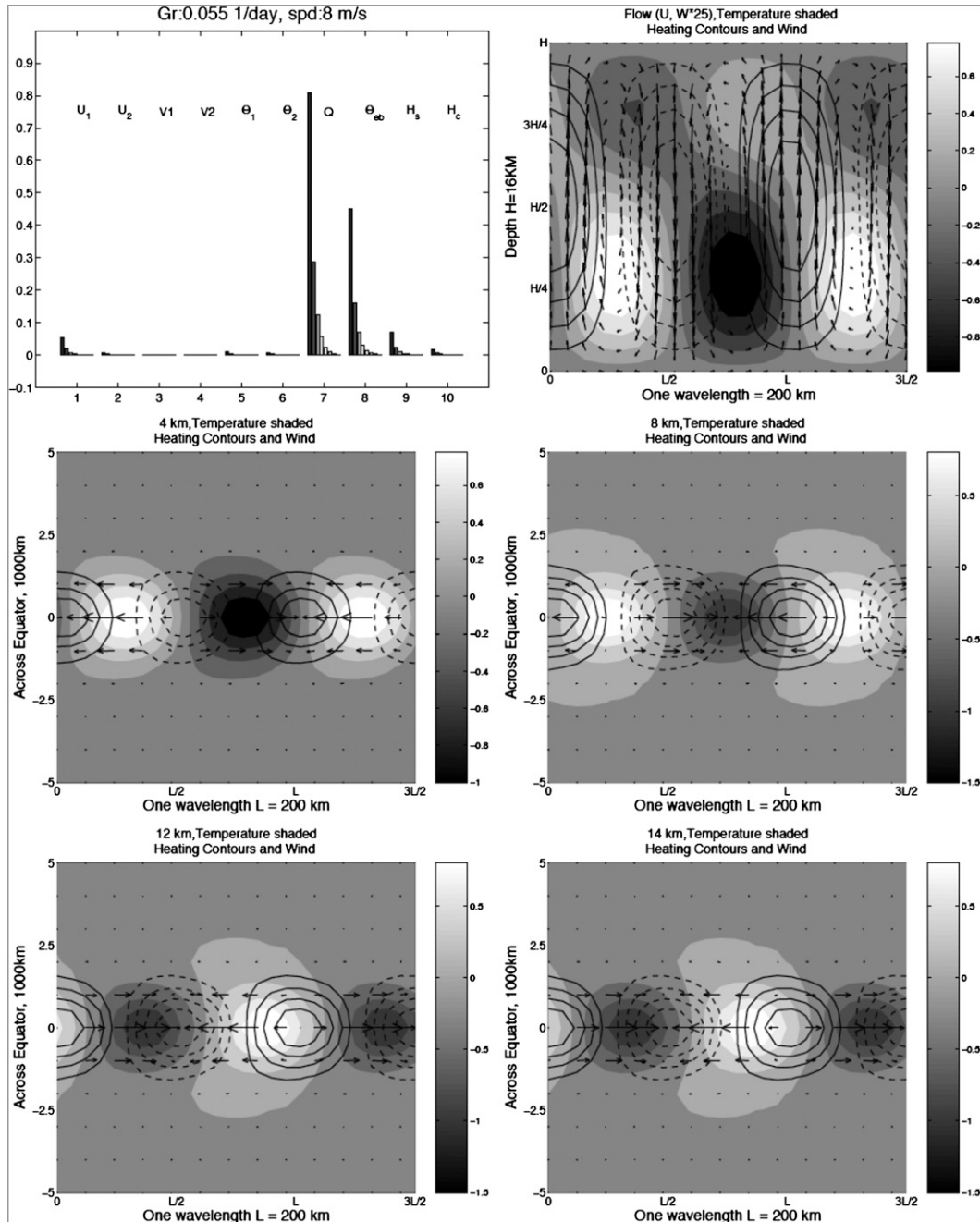


FIG. 4. Dynamical and physical structure of the squall line-like wave associated with the strong WWB regime of the MS09 background ($t = 1000$ days); $\bar{U}_1 = 7.67 \text{ m s}^{-1}$ and $\bar{U}_3 = -1.67 \text{ m s}^{-1}$. (top left) Bar diagram showing the strength of meridional components of dynamical variables; (top right) (x, z) contours of meridional average. (middle),(bottom) Horizontal and zonal structure and various heights.

vertical shears that closely mimics the reanalysis MJO profiles taken from Tromeur and Rossow (2010). However, because the background wind is not the only environmental variable that varies during the passage of the MJO, here we extend the analysis to variations in the moisture profile as well. Similarly, we consider a tilted profile that mimics the

MJO humidity plots from Tromeur and Rossow (2010). This is considered in section 3b below.

a. Sensitivity to the moisture profile

Before we consider an MJO scenario where both the moisture and wind profile evolve together, we look at

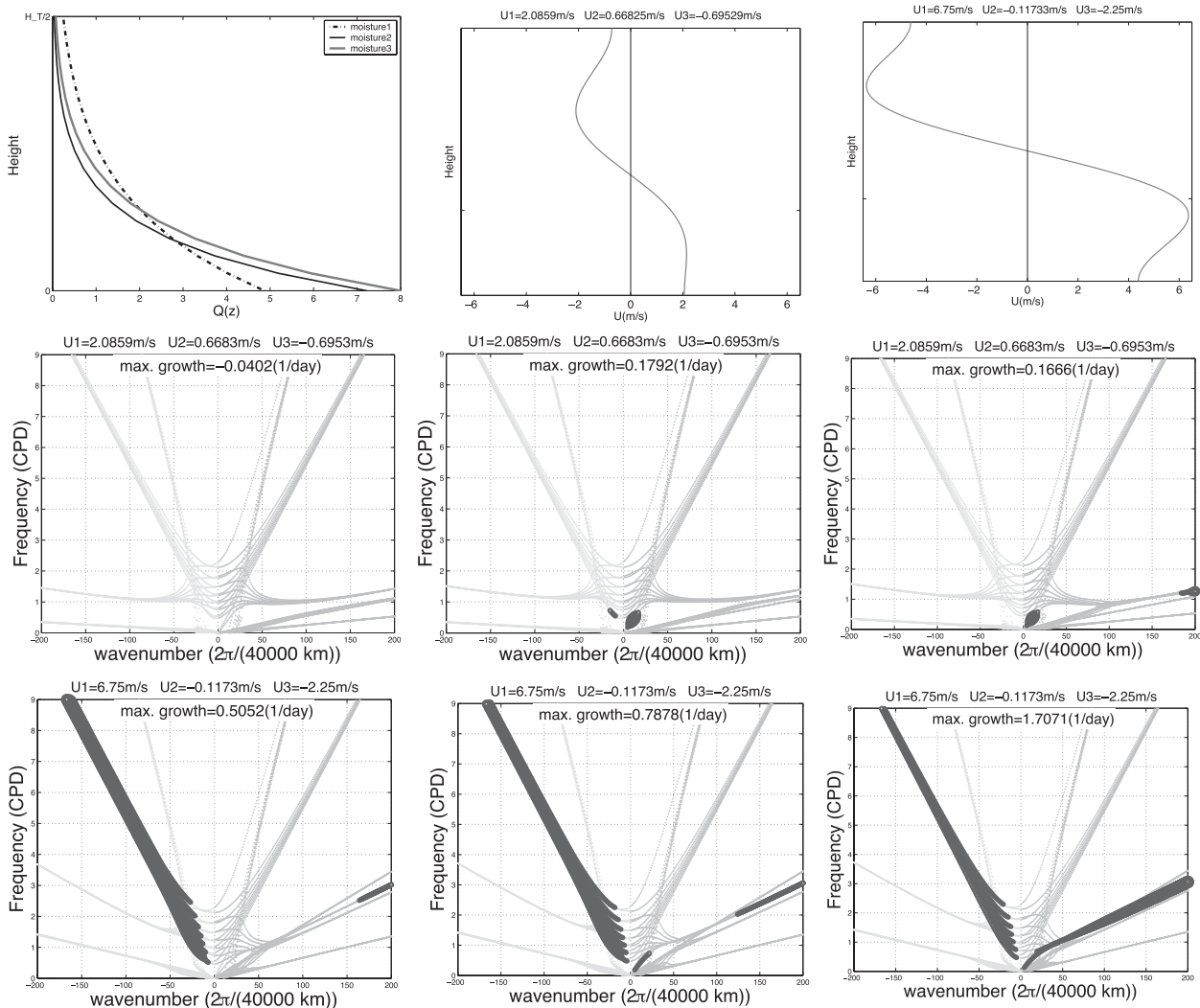


FIG. 5. Sensitivity to the moisture background. (top) Moisture and WW profiles. (middle),(bottom) Dispersion relations and instability diagrams for the moisture profiles 1–3 and the intermediate and strong westerly shears, respectively.

the sensitivity of the model to changes in the moisture profile, for two different shear strengths, during the WWB phase. Namely, we consider three moisture profiles that represent roughly the three main phases of the MJO: dry below and moist aloft; moist below and dry aloft; and a somewhat moister below profile, yielding a stronger moisture gradient overall, corresponding respectively to profiles 1, 2, and 3 shown on the top of Fig. 5 together with the two westerly shears corresponding roughly to the onset and mature phases of the WWB.

It is important to note here that it is actually the gradient of the moisture background that affects the model stability feature and not the moisture content in the lower and/or upper troposphere. In fact, the variations in moisture profile affect the multicloud model equations in (2) through changes in the moisture convergence

parameters \tilde{Q} and $\tilde{\lambda}$ that appear in the q equation. To find adequate moisture parameters, we consider moisture background profiles of the form $Q(z) = q_0 e^{-z/H_q}$, where H_q and q_0 are “fitting” parameters representing the moisture scale height and the value of moisture at the top of the boundary layer, respectively (Khouider and Majda 2006). For instance the lag -6 and lag -3 profiles in Fig. 4 correspond respectively to exponential profiles with $q_0 = 7.22$ K and $H_q/H_T = 0.0799, 0.09615$, respectively, yielding the coefficient values $\tilde{Q} = 0.7677, \tilde{\lambda} = 0.849$ and $\tilde{Q} = 0.9, \tilde{\lambda} = 0.8$, respectively. We note that the latter case corresponds to the default values used in Khouider and Majda (2006, 2008a,b), MS09, and HK10 and in the previous section. The values of \tilde{Q} and $\tilde{\lambda}$ for the rest of the moisture profiles used in this paper are summarized in Table 3.

TABLE 3. Moisture profiles used.

Profile	Figure	\tilde{Q}	$\tilde{\lambda}$
Moisture 1	5	0.9031	0.6047
Moisture 2	5	0.9	0.8
Moisture 3	5	1.0382	0.7846
Lag -6	6	0.7677	0.849
Lag -3	6	0.9	0.8
Lag -2	6	1.0382	0.7846
Lag 0	6	1.0837	0.7679
Lag +2	6	0.7787	0.7846
Lag +4	6	0.6811	0.83
Lag +9	6	0.6378	0.849

The dispersion diagrams corresponding to these three moisture and two wind shear profiles are shown in the middle and bottom panels of Fig. 5. We note that the MJO vertical shear background in Fig. 4 includes a non-zero second baroclinic component U_2 , unlike the MS09 background from the previous section. However, U_2 remains relatively small compared to U_1 and U_3 .

From Fig. 5, we see that, in the weak shear environment, the multicloud model is stable when the low-level troposphere is dry and in the strong shear the overall growth rates increase as the low-level troposphere moistens. While the WIG waves are stable in the weak shear case, independent of the background moisture, the Kelvin and squall line-like waves are the most affected by the changes in the background moisture in both the weak and strong shears. However, while both Kelvin waves and squall lines are effectively stabilized when the lower troposphere is dry below and moist aloft, the squall lines are more sensitive to changes in the moisture gradient; in the strong shear case, shown in the bottom panels of Fig. 5, the increase in growth rates for the squall line-like waves, as the moisture profile evolves from profiles 1 through 3, is considerably larger than that of the Kelvin wave, although the latter appears to be stable in the bottom-left panel.

The physical mechanisms at work can be summarized as follows. The variations in background wind induce strong changes in both lower-level and midlevel shear. The mid-level shear stretches the stratiform anvils and affects the stability properties of the model by enhancing the growth rates, although the dry model (i.e., when the convective heating is turned off) remains stable in the presence of the shear as demonstrated in HK10. The lower-level shear, on the other hand, affects the congestus clouds and thus the moisture preconditioning. Likewise, the moisture gradient affects directly the moisture convergence through variations of the parameters \tilde{Q} and $\tilde{\lambda}$ in the q equation in (2).

b. The MJO background

In Fig. 6, we plot reconstructed profiles of the observed MJO zonal wind anomalies (Tromeur and Rossow 2010),

using the three first vertical modes of vertical structure, and the moisture background based on the exponential form above with a sequence of parameters q_0 and H_q that best mimic the MJO filtered specific humidity from the above cited paper. In Fig. 6, the sequence of moisture profiles is separated into two panels for clarity. In a nutshell, the moisture profile evolves from a lower troposphere that is moist near the surface (the boundary layer) and dry aloft during the MJO onset phase (in front; lag -6 and lag -3) to a profile that is moister both near the surface and aloft during the initiation and mature deep convection phases (in the middle; lag -2 and lag 0), and then moist aloft and dry below during the stratiform phase (in the rear; lag +4 and lag +9).

The sequence of moisture profiles in Fig. 6 corresponds to a progressive moistening near the surface during the inactive phase that triggers a progressive moistening aloft during the onset and through the initiation phases. While moistening aloft continues, during the early stage of the active phase, the moisture profile becomes progressively drier near the surface.

4. Multiscale waves in the MJO envelope

In Figs. 7a–i, we present a sequence of dispersion diagrams that represent variations in the background vertical shear and moisture profile as the MJO envelope evolves from its onset phase to its decay as illustrated in Fig. 6. Figure 7 suggests a certain organization of a menagerie of synoptic and mesoscale waves within the MJO envelope depending on the various phases of the MJO. With the lag -6 wind shear and moisture profile (moist below and dry aloft), corresponding roughly to the MJO onset phase, Fig. 7a suggests an MJO background favorable mostly to eastward-moving waves, comprised of synoptic-scale EIG and Kelvin waves as well as mesoscale second baroclinic waves, that would zip quickly through and exit the MJO region. As summarized in Table 4, Kelvin (and EIG) waves tend to have large growth rates in front of the MJO and weak in the back, while WIG waves are strong in the back and stable in front. In the convection core (lag 0 wind and moisture profiles), both Kelvin and WIG waves coexist together with mesoscale squall line-like waves. Squall lines appear at lag -3 and progressively become dominant and prominent throughout the active phase between lag -2 and lag 0. They change their direction of propagation as the WWB develops near the surface. Mesoscale dry second baroclinic modes propagate eastward in front of the MJO and westward in the back, following the direction of the third baroclinic wind near the surface and near the top of the troposphere (as demonstrated by sensitivity tests not included here).

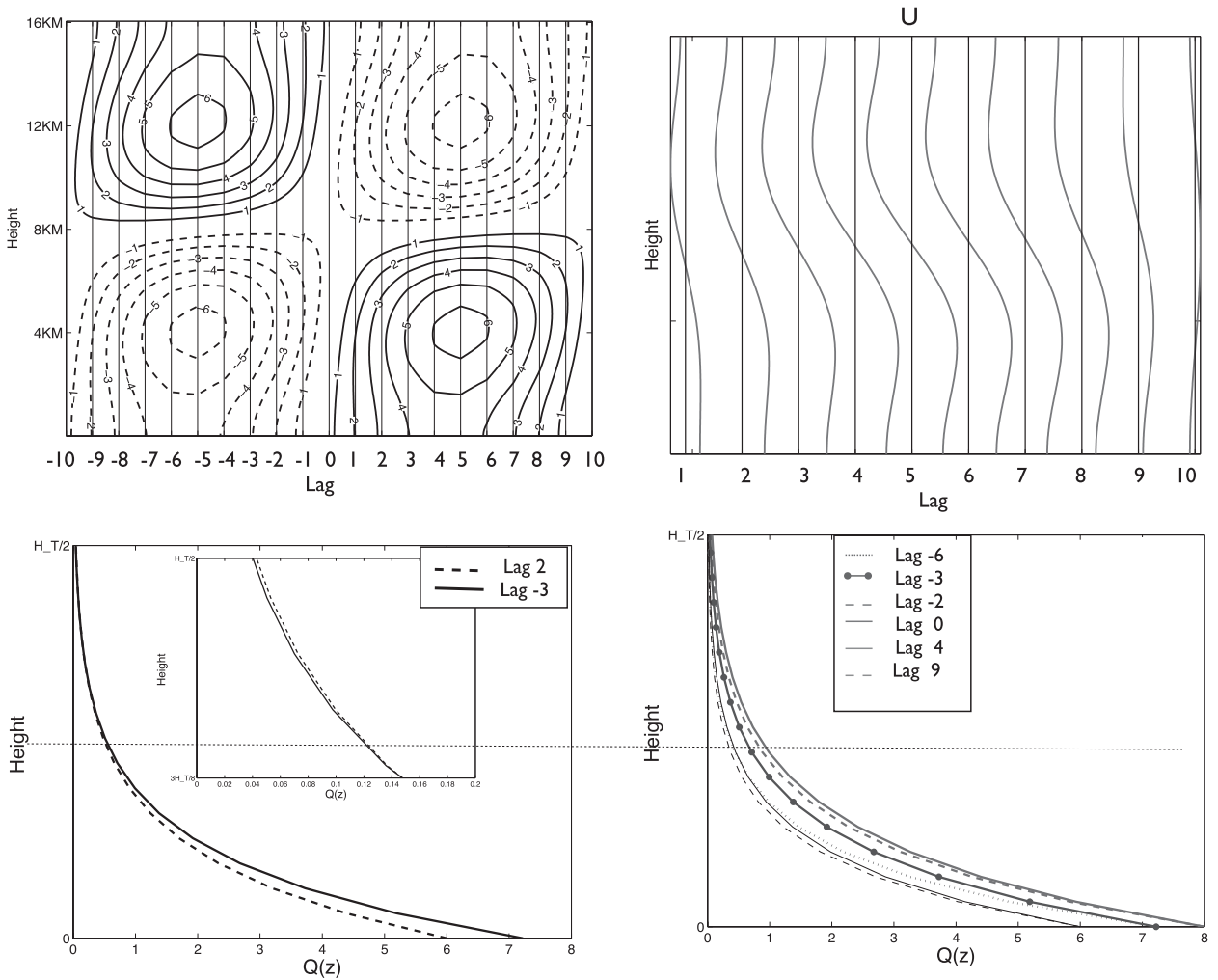


FIG. 6. MJO background profile. (top left) Lag–height contours of the zonal wind. An easterly wind shear (EW) during the inactive-onset phase is followed by a westerly shear (WW) during the active phase. (top right) A sequence of the vertical shear profiles during the active phase. (bottom) A sequence of moisture background profiles during various phases of the MJO roughly mimicking the humidity profile from observational data. The lag unit in the zonal wind panels is roughly 2–3 days while in the moisture panels the lag unit is roughly 5–7 days.

As the lower troposphere moistens progressively, near and above the surface, the multicloud model instability gives rise to squall line–like mesoscale waves that move westward in the direction of the low-level wind. In Fig. 7d, corresponding to the lag –2 profiles, with a relatively weak background shear, the squall line–like mode already dominates the instability, although both the Kelvin (and EIG) waves and mesoscale second baroclinic waves still have substantial growth rates. The overall instability then decreases as the shear strength decreases near the convection center (lag 0 moisture profile) and gives rise to both Kelvin waves and squall line–like waves, which appear to move westward in Fig. 7e and eastward in Fig. 7f.

As the WWB strengthens, the growth rates of the (eastward-moving) squall lines increase substantially

while at the same time it still sustains Kelvin waves; it also exhibits WIG and mesoscale westward second baroclinic gravity waves (Fig. 7g). However, as the lower troposphere becomes drier, especially near the surface (lag +2), the squall lines’ instability disappears, and WIG and second baroclinic mesoscale waves become more dominant (Fig. 7h). Finally, when both the lower troposphere is dry and the WWB is weak, the mesoscale second baroclinic waves become stable and the overall instability weakens substantially.

Implications for CMT feedback

Starting from the general idea that westward-tilted waves typically accelerate westerly shears and decelerate (low-level) easterly shears while eastward-tilted waves accelerate easterlies shears and decelerate (low-level)

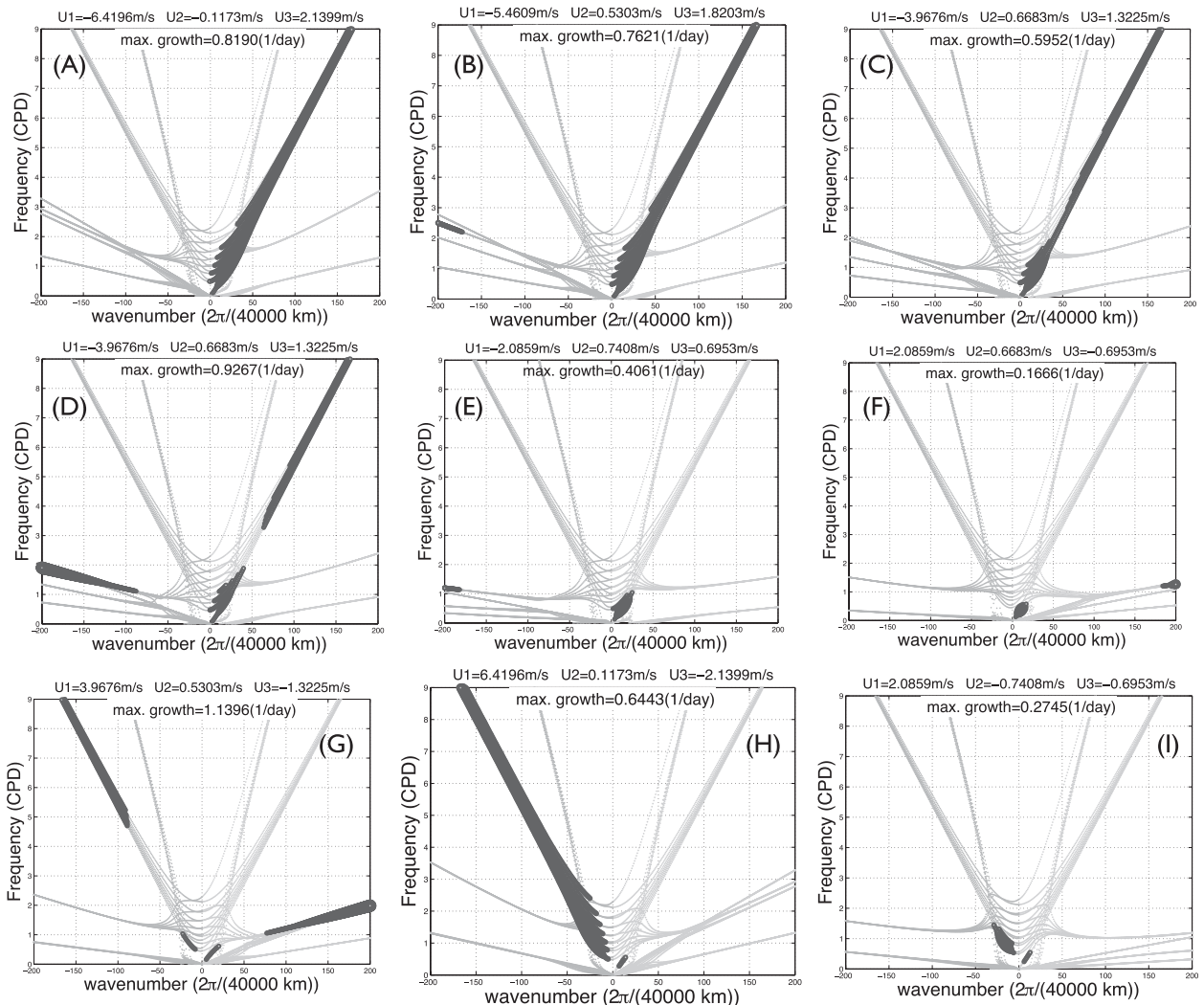


FIG. 7. Multiscale waves in the MJO background. Sequence of background winds combined with a sequence of moisture profiles representing the evolution within the MJO envelope from the onset to decay as illustrated in Fig. 4: (a) lag -6 , (b) lag -3 , (c) wind lag -2 and moisture lag -3 , (d) lag -2 , (e) wind lag -1 and moisture lag -2 , (f) wind lag $+1$ and moisture lag 0 , (g) wind lag $+2$ and moisture lag 0 , (h) lag $+4$, and (i) lag $+9$.

westerly shears (Majda and Biello 2004; MS09), here we speculate about the CMT implication, for the MJO envelope itself, from the predisposition of the multiscale waves in Figs. 7a–i. We note here that westward-tilted waves (i.e., east to west in the vertical direction), typically moving eastward, comprise Kelvin and EIG waves and squall lines, in a westerly shear background (easterly wind above westerly wind), while eastward-tilted waves, typically moving westward, include WIG waves and squall lines in an easterly background shear.

We are not trying here to come up with a theory for MJO initiation and or dynamics but rather to simply speculate about plausible CMT feedback scenarios from synoptic and mesoscale CCWs embedded within the MJO envelope to warrant future investigations

using observations and/or numerical simulations. Moreover, while as revealed by linear analysis for the simulation of MS09 reported in Fig. 1, positive growth rates do not necessarily imply a mature phase of the corresponding wave (i.e., there is some time lag between the two), our speculations are based solely on the growth rates. Nonetheless, the associated time lags are much smaller than the MJO time scale.

Table 5 and Fig. 8 summarize the plausible CMT feedback scenario due to the synoptic CCWs and mesoscale squall line-like waves that are favored within each region of the MJO envelope. We note that Table 5 and Fig. 8 refer only to Kelvin and WIG waves, in addition to squall lines. While the present model suggests instabilities of higher-order EIG and WIG waves, only

TABLE 4. Multiscale waves within the MJO envelope. Here A–I indicate Figs. 6a–i, respectively. Lower-case “lag” follows the sequence of moisture profiles and upper-case “Lag” is for the wind profiles in Fig. 6. The maximum growth rate (day^{-1}) is shown in parentheses after the wave name. E/W 2nd: eastward/westward mesoscale 2nd baroclinic gravity wave. E/W SQLN: eastward/westward squall line–like mesoscale wave.

I: lag +9, Lag +9	H: lag +4, Lag +4	G: lag 0, Lag +2	F: lag 0, Lag +1	E: lag -2, Lag -1	D: lag -2, Lag -2	C: lag -3, Lag -2	B: lag -3, Lag -3	A: lag -6, Lag -3
Kelvin (0.052)	Kelvin (0.045)	Kelvin (0.17)	Kelvin (0.17)	Kelvin (0.41)	Kelvin (0.58)	Kelvin (0.59)	Kelvin (0.76)	Kelvin (0.82)
WIG (0.27)	WIG (0.64)	WIG (0.163)		EIG (0.16)	EIG (0.37)	EIG (0.4)	EIG (0.57)	EIG (0.65)
	W 2 nd (0.44)	W 2 nd (0.2)			E 2 nd (0.22)	E 2 nd (0.2)	E 2 nd (0.4)	E 2 nd (0.46)
		E SQLN (1.14)	E SQLN (0.13)	W SQLN (0.15)	W SQLN (0.926)	W SQLN (0.08)		

Kelvin and symmetric $N = 1$ WIG waves are observed in nature (Wheeler and Kiladis 1999; Kiladis et al. 2009). One possibility is that the Kelvin and WIG waves are the most prominent CCWs in nature and thus the most statistically significant. This is somewhat reflected in the model results given that EIG waves always appear together with Kelvin waves and never alone and they always have smaller growth rates than the latter. Moreover, it is not clear whether a weak EIG wave can survive the passage of a strong Kelvin wave because the latter may use up all of the resources (CAPE and moisture) and “starve” the former to “death.”

The (dry) second baroclinic gravity waves are ignored in this CMT discussion because on the one hand there is no observational evidence for their existence and consistently there are not seen in the MS09 simulation, discussed in section 2, and on the other hand they always appear as a continuation of the instabilities of the EIG or WIG waves on the corresponding dispersion relation branches, in Fig. 7.

The MJO envelope is divided into five main CMT regions. East of the convection core, we find the preconditioning region that we generically call the onset region. It is the region of the MJO envelope where the MJO wind anomalies are dominated by strong easterlies below westerlies (i.e., an easterly shear), where, on the MJO scale, the low-level troposphere is relatively dry

compared to the planetary boundary layer but is progressively moistening by detrainment of congestus clouds and the associated low-level large-scale convergence. According to the model results in Fig. 7, this region favors eastward-moving CCWs such as Kelvin and EIG waves, which that would zip quickly in front and leave the MJO envelope, and squall line–like waves that move with the low-level wind (i.e., westward), toward the MJO convection core. Accordingly, the eastward CCWs (Kelvin waves in particular) would then induce a deceleration of MJO background easterly shear while the squall lines would tend to accelerate it. However, in this region of the MJO envelope, corresponding roughly to Figs. 7a–c, the growth rates are dominated by Kelvin and eastward-moving waves; in general, we therefore expect deceleration by eastward-moving waves to dominate acceleration by the squall lines.

West of the onset region, the mature phase is divided into two subregions: one located east of the convection core, where the easterly shear has weakened a lot (due in part to Kelvin wave activity during the onset phase) and the other located west of the core, where a westerly shear starts to form and grow (the onset phase of the WWB). The east-of-the-core region, corresponding roughly to Figs. 7d and 7e, is characterized by Kelvin waves and westward-moving squall lines. In this region, the growth rates of the eastward-moving waves and the

TABLE 5. Plausible CMT feedback scenario from MJO background induced by synoptic-scale convectively coupled waves and squall lines. Here A–I refer to Figs. 6a–i, respectively. Note that the effect of waves emanating from other sources is not taken into account here.

MJO phase/waves	Onset (A–C)	East of core (D, E)	West of core (F, G)	Mature WWB (H)	Decaying WWB (I)
WIG	N/A	N/A	N/A	Deceleration	Deceleration
Kelvin	Deceleration	Deceleration	Acceleration	Acceleration	Acceleration
SQLN	Acceleration	Acceleration	Acceleration	Acceleration	N/A
Total CMT effect	Deceleration of easterlies by Kelvin waves	Neutral	Acceleration of WWB by Kelvin waves and squall lines	Deceleration of WWB by WIG waves	Deceleration by WIG waves continues and would potentially trigger acceleration of easterlies for next MJO event.

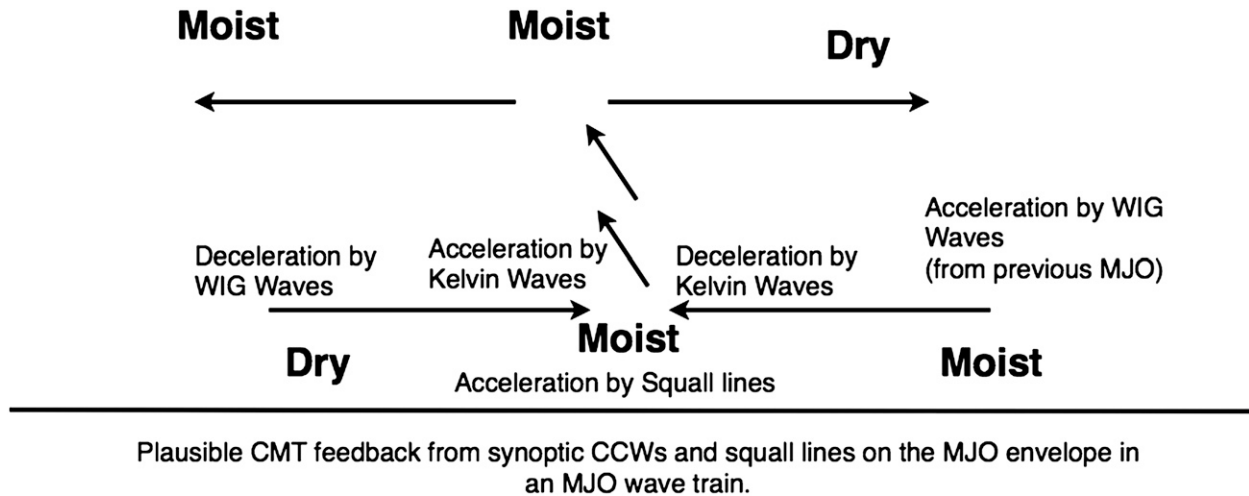


FIG. 8. A schematic of the plausible multiscale two-way interaction between the MJO envelope and embedded synoptic-scale CCWs and squall lines as suggested by the model results.

westward squall lines are more or less comparable. In fact, the squall lines appear to slightly dominate in Fig. 7d. Thus we expect the overall CMT feedback effect to be neutral.

The WWB onset region, west of the core, starts in Fig. 7f with both Kelvin waves and eastward-moving squall lines that both accelerate the freshly formed WWB and finishes in Fig. 7g where Kelvin and squall lines coexist with WIG waves. However, in Fig. 7g, while the maximum growth rate of WIG waves is comparable to that of Kelvin waves (0.163 and 0.17 day^{-1} , respectively, according to Table 4), that of the squall lines is almost 10 times larger (1.14 day^{-1} , according to Table 4). Therefore, the WWB that was first accelerated due to Kelvin waves [consistent with the hypothesis of Majda and Biello (2004)] continues to accelerate due to the prevalence of squall lines, when WIG waves start to form (and compensate the acceleration due to Kelvin waves). When the WWB gets stronger (Fig. 7h), the WIG waves will dominate the scenery and therefore induce a net deceleration of the background westerly shear and lead to the demise of the MJO in Fig. 7i.

Finally, we note that Fig. 8 suggests the possibility for the MJO onset region to be accelerated by WIG waves emanating from the tail of a preceding MJO in the event of a train of MJOs, which seems to be very common in nature (Yanai et al. 2000).

5. Concluding summary and discussion

The two-way interactions between synoptic and meso-scale CCWs in an MJO-like planetary-scale background was investigated here using the multcloud model framework of Khouider and Majda (2006, 2008a,b).

The WWB background obtained by a simple multiscale model (MS09) is used here to perform linear stability analysis for the multcloud model on an equatorial beta plane, using Galerkin expansions in the meridional direction, following HK10. Consistent with the results of MS09, the strong WWB regime favors WIG and squall line-like waves while the weak WWB regime favors Kelvin waves, as shown in Fig. 2. To highlight the role of rotation effects in breaking the symmetry between east and west, which are ignored in the MS09 model, we considered in Fig. 3 the negative of the westerly background of MS09. We found that both the strong and weak easterly shear regimes favor EIG and Kelvin waves, consistent with the work of HK10, although in HK10 the third baroclinic wind component was not included in the background shear. Although similar to the WWB case, westward-moving squall line-like waves develop when the easterly shear is strong. To be more pragmatic, the WWB background is viewed as the active phase or the back side and its negative as the onset or front side of the MJO envelope where synoptic and mesoscale CCWs evolve and interact with the MJO.

For more realism, we thus considered in section 3 rough approximations of the evolving sequences of MJO zonal wind and moisture profiles, based respectively on the three first baroclinic modes and a heuristic exponential profile, from reanalysis data (Tromeur and Rossow 2010). It is found in section 3 that the stability diagram of the multcloud model is sensitive to variations in the moisture profile and the squall lines, in particular, are favored by bottom-heavy moisture profiles that prevail in the convection core of the MJO.

The types of synoptic and mesoscale CCWs that are excited in various regions of the MJO when both

variations in zonal wind and moisture profiles are considered together are discussed in section 4. It is found that the onset region, which is characterized by a strong easterly shear and a moisture profile that moist below and dry aloft, is favorable for Kelvin and EIG waves that propagate eastward in front of the MJO. East of the convection core, which is characterized by a weak easterly shear and an overall moist lower troposphere, favors both Kelvin waves and squall line–like waves that move westward toward the convection center, although the squall line waves have larger growth rates (Fig. 7g and Table 4). West of the core, the region of WWB onset is dominated by both Kelvin waves and eastward-moving squall lines. This sudden transition between westward- and eastward-propagating squall line–like mesoscale systems is consistent with the results of Grabowski (1998), who documented the evolution of mesoscale convective clusters during the TOGA COARE experiment using both radar data and CRM simulations.

The mature phase of WWB, which still has a moist lower-to-middle troposphere, is dominated by WIG waves but both Kelvin and squall line–like waves are still unstable. The stratiform wake of the MJO is characterized by a weaker westerly shear and a moist over dry moisture profile. It yields WIG waves and Kelvin waves. The persistence of WIG waves within the WWB regions is consistent with the observational study of Chen et al. (1996), who showed that westward propagation inertio-gravity waves with a 2-day period are predominant within the active phase of the TOGA COARE MJO.

Using the general CMT theory that states that westward-tilted waves accelerate the westerly shear and eastward-tilted waves accelerate easterly shears, we can speculate about the plausible CMT feedback due to the synoptic-scale CCWs and the mesoscale squall line–like waves embedded within each region of the MJO envelope. Accordingly, the Kelvin and EIG waves in front of the MJO are expected to decelerate the easterly shear while the squall lines east of the convection core provide an acceleration that would likely compensate and retard the deceleration caused by Kelvin waves. Kelvin waves and eastward-moving squall lines that prevail on the western flank of the convection core would accelerate the WWB and likely contribute to its onset while WIG waves that dominate the mature WWB phase cause its deceleration. This WIG deceleration likely continues throughout the stratiform wake and would cause the demise of the WWB. This is partly consistent with the work of Houze et al. (2000), who reported that the transition from the “westerly onset” to the “westerly wind burst” phases of the MJO wave is characterized by midlevel easterlies

overlying low-level westerlies and low-level westerlies expanding to midlevel, which occur within the MJO convective core. They argued that this results in the development of convective systems that, through CMT, decelerate the easterly midlevel jet within the westerly onset region and the acceleration of the westerly jet within the WWB region.

The suggested deceleration of the WWB due to CMT from westward-moving waves and its acceleration by eastward-moving waves is in essence a dynamical mechanism that is consistent with the eastward propagation and maintenance of the MJO. The deceleration of the easterly shear and acceleration of the WWB by Kelvin waves within the MJO onset and mature phases, respectively, and the deceleration of the WWB by WIG waves in the back of the MJO envelope could arguably contribute to the eastward propagation of the MJO. Moreover, as demonstrated in the simulations of Khouider et al. (2012), mesoscale CMT can act directly on both the synoptic-scale CCWs and their planetary-scale envelopes; mesoscale CMT from squall lines may thus provide a compensation for the deceleration of the MJO winds by WIG and Kelvin waves, on each side of the core, respectively, to maintain the MJO strength near the convective center.

While the present study demonstrates, somewhat heuristically, using a simple model, the importance of both moisture and background wind for the multiscale interactions between synoptic and mesoscale waves, more work needs to be done in order to fully elucidate and understand the effect of moisture and other variables in this multiscale process.

Acknowledgments. The research of B.K is support in part by the Natural and Engineering Research Council of Canada and the Canadian Foundation for Climate and Atmospheric Sciences (CFCAS). Y.H. is supported as a PDF through B.K’s CFCAS grant. A.M. is supported in part by ONR Grant N00014-11-1-0306, ONR-DRI Grant N00014-10-1-0554, NSF Grant DMS-0456713, and NSF-CMG Grant DMS-1025468, and S. S. is supported by an NSF Mathematical Sciences Postdoctoral Research Fellowship and a start-up grant from the University of Wisconsin—Madison.

REFERENCES

- Biello, J., and A. Majda, 2005: A multiscale model for the Madden-Julian oscillation. *J. Atmos. Sci.*, **62**, 1694–1721.
- Chen, S. S., R. A. Houze Jr., and B. E. Mapes, 1996: Multiscale variability of deep convection in relation to large-scale circulation in TOGA COARE. *J. Atmos. Sci.*, **53**, 1380–1409.
- Dudhia, J., M. W. Moncrieff, and D. W. K. So, 1987: The two-dimensional dynamics of West African squall lines. *Quart. J. Roy. Meteor. Soc.*, **113**, 121–146.

- Grabowski, W. W., 1998: Toward cloud resolving modeling of large-scale tropical circulations: A simple cloud microphysics parameterization. *J. Atmos. Sci.*, **55**, 3283–3298.
- Haertel, P. T., and R. H. Johnson, 1998: Two-day disturbances in the equatorial western Pacific. *Quart. J. Roy. Meteor. Soc.*, **124**, 615–636.
- Han, Y., and B. Khouider, 2010: Convectively coupled waves in a sheared environment. *J. Atmos. Sci.*, **67**, 2913–2942.
- Houze, R. A. J., S. S. Chen, D. E. Kingsmill, Y. Serra, and S. E. Yuter, 2000: Convection over the Pacific warm pool in relation to the atmospheric Kelvin–Rossby wave. *J. Climate*, **57**, 3058–3089.
- Johnson, R. H., T. M. Rickenbach, S. A. Rutledge, P. E. Ciesielski, and W. H. Schubert, 1999: Trimodal characteristics of tropical convection. *J. Climate*, **12**, 2397–2418.
- Khouider, B., and A. J. Majda, 2006: A simple multicloud parameterization for convectively coupled tropical waves. Part I: Linear analysis. *J. Atmos. Sci.*, **63**, 1308–1323.
- , and —, 2008a: Equatorial convectively coupled waves in a simple multicloud model. *J. Atmos. Sci.*, **65**, 3376–3397.
- , and —, 2008b: Multicloud models for organized tropical convection: Enhanced congestus heating. *J. Atmos. Sci.*, **65**, 895–914.
- , Y. Han, and J. Biello, 2012: Convective momentum transport in a simple multicloud model. *J. Atmos. Sci.*, **69**, 281–302.
- Kiladis, G. N., K. H. Straub, and P. T. Haertel, 2005: Zonal and vertical structure of the Madden–Julian oscillation. *J. Atmos. Sci.*, **62**, 2790–2809.
- , M. C. Wheeler, P. T. Haertel, K. H. Straub, and P. E. Roundy, 2009: Convectively coupled equatorial waves. *Rev. Geophys.*, **47**, RG2003, doi:10.1029/2008RG000266.
- Lane, T. P., and M. W. Moncrieff, 2010: Characterization of momentum transport associated with organized moist convection and gravity waves. *J. Atmos. Sci.*, **67**, 3208–3225.
- LeMone, M. A., 1983: Momentum transport by a line of cumulonimbus. *J. Atmos. Sci.*, **40**, 1815–1834.
- , and M. W. Moncrieff, 1994: Momentum and mass transport by convective bands: Comparisons of highly idealized dynamical models to observations. *J. Atmos. Sci.*, **51**, 281–305.
- , E. J. Zipser, and S. B. Trier, 1998: The role of environmental shear and thermodynamic conditions in determining the structure and evolution of mesoscale convective systems during TOGA COARE. *J. Atmos. Sci.*, **55**, 3493–3518.
- Lin, X., and R. H. Johnson, 1996: Kinematic and thermodynamic characteristics of the flow over the western Pacific warm pool during TOGA COARE. *J. Atmos. Sci.*, **53**, 695–715.
- Liu, C., and M. W. Moncrieff, 1996: Mass and momentum transports by organized convection: Effects of shear and buoyancy. *J. Atmos. Sci.*, **53**, 964–979.
- Madden, R., and P. Julian, 1971: Detection of a 40–50-day oscillation in the zonal wind in the tropical Pacific. *J. Atmos. Sci.*, **28**, 702–708.
- , and —, 1972: Description of global-scale circulation cells in the tropics with a 40–50-day period. *J. Atmos. Sci.*, **29**, 1109–1123.
- Majda, A. J., 2003: *Introduction to PDEs and Waves for the Atmosphere and Ocean*. American Mathematical Society, 234 pp.
- , and J. Biello, 2004: A multiscale model for tropical intraseasonal oscillations. *Proc. Natl. Acad. Sci. USA*, **101**, 4736–4741.
- , and S. N. Stechmann, 2008: Stochastic models for convective momentum transport. *Proc. Natl. Acad. Sci. USA*, **105**, 17 614–17 619.
- , and —, 2009a: The skeleton of tropical intraseasonal oscillations. *Proc. Natl. Acad. Sci. USA*, **106**, 8417–8422.
- , and —, 2009b: A simple dynamical model with features of convective momentum transport. *J. Atmos. Sci.*, **66**, 373–392.
- Mapes, B., S. Tulich, J. Lin, and P. Zuidema, 2006: The mesoscale convection life cycle: Building block or prototype for large-scale tropical waves? *Dyn. Atmos. Oceans*, **42**, 3–29.
- Matsuno, T., 1966: Quasi-geostrophic motions in the equatorial area. *J. Meteor. Japan*, **44**, 25–43.
- Moncrieff, M. W., 1981: A theory of organized steady convection and its transport properties. *Quart. J. Roy. Meteor. Soc.*, **107**, 29–50.
- , 1992: Organized convective systems: Archetypical dynamical models, mass and momentum flux theory, and parametrization. *Quart. J. Roy. Meteor. Soc.*, **118**, 819–850.
- , and E. Klinker, 1997: Organized convective systems in the tropical western Pacific as a process in general circulation models: A TOGA COARE case-study. *Quart. J. Roy. Meteor. Soc.*, **123**, 805–827.
- Nakazawa, T., 1988: Tropical super clusters within intraseasonal variation over the western Pacific. *J. Meteor. Soc. Japan*, **66**, 823–839.
- Roundy, P., 2008: Analysis of convectively coupled Kelvin waves in the Indian Ocean MJO. *J. Atmos. Sci.*, **65**, 1342–1359.
- Tromeur, E., and W. B. Rossow, 2010: Interaction of tropical deep convection with the large-scale circulation in the MJO. *J. Climate*, **23**, 1837–1853.
- Tung, W.-W., and M. Yanai, 2002a: Convective momentum transport observed during the TOGA COARE IOP. Part I: General features. *J. Atmos. Sci.*, **59**, 1857–1871.
- , and —, 2002b: Convective momentum transport observed during the TOGA COARE IOP. Part II: Case studies. *J. Atmos. Sci.*, **59**, 2535–2549.
- Wheeler, M., and G. N. Kiladis, 1999: Convectively coupled equatorial waves: Analysis of clouds and temperature in the wavenumber–frequency domain. *J. Atmos. Sci.*, **56**, 374–399.
- Wu, X., and M. Yanai, 1994: Effects of vertical wind shear on the cumulus transport of momentum: Observations and parameterization. *J. Atmos. Sci.*, **51**, 1640–1660.
- , and M. W. Moncrieff, 1996: Collective effects of organized convection and their approximation in general circulation models. *J. Atmos. Sci.*, **53**, 1477–1495.
- Yanai, M., B. Chen, and W. Tung, 2000: The Madden–Julian oscillation observed during the TOGA COARE IOP: Global view. *J. Atmos. Sci.*, **57**, 2374–2396.